Phase field simulation of martensitic-transformation-induced plasticity in steel

Rajeev Ahluwalia [ORCID],[*] Jakub Mikula [ORCID], Robert Laskowski [ORCID], and Siu Sin Quek [ORCID]
Institute of High Performance Computing, A*STAR, Singapore 138632, Singapore

The influence of martensitic-transformation-induced plastic deformation in steel is studied using phase field simulations. A phase field framework that incorporates elastic as well as plastic effects is used. A high-carbon steel is considered as an example to illustrate the coupling of martensitic transformations and plasticity. In this work, all 24 transformation variants associated with the Kurdjumov-Sachs orientational relationship are considered to realistically describe the martensitic transformation in steel. Temperature-induced as well as stress-induced transformations are studied. The role of plasticity is investigated by performing simulations with and without the plastic flow. It is found that transformation plasticity plays a dual role: (1) in the case of temperature-induced transformations it helps in the initial nucleation of the martensite by stabilizing the initial embryo, and (2) once the martensite starts to grow, transformation-induced plasticity resists the further growth and results in stabilization of retained austenite. In contrast, the simulations in the absence of transformation-induced plasticity show that the entire system transforms into martensite. For stress-induced transformations, it is found that transformation induces plastic deformations, even though the applied (macroscopic) stress is lower than the yield stress. Although the dominant contribution to the stress-induced strain arises due to the formation of favored martensite variants, transformation-induced plasticity generates significant additional deformation that can influence the mechanical properties and the resulting martensite domain pattern.

I. INTRODUCTION

Martensitic transformation in steel is an important phase transformation that is often exploited to increase the hardness [1]. Rapid quenching from the face-centered-cubic (fcc) austenite phase leads to the formation of a body-centered-tetragonal (bct) martensite structure. The martensitic transformation is a diffusionless phase transformation that leads to a shape change of the unit cell. The elastic energy generated due to the shape-changing transformation significantly influences the final microstructure of the martensite. Accommodation of the elastic energy is often achieved by formation of internally twinned martensite plates, such that an invariant habit plane is obtained [2]. Such a morphology is usually observed in steels with high carbon contents [3]. Another mechanism, usually associated with low-carbon steels, is that of elastic energy accommodation by slip, leading to the formation of lath martensite [3]. Thus, both elastic and plastic effects play an important role during martensitic transformations in steel. In fact, steels that exhibit transformation-induced plasticity (TRIP) have been shown to lead to a good combination of strength and ductility [4]. The understanding of the interplay between martensitic transformations and plasticity in steel is therefore very important [4–6].

There are two fundamental mechanisms associated with transformation-induced plasticity: (1) the Greenwood-Johnson [7] mechanism by which the deformation associated with the martensitic transformation leads to plastic flow in the weaker austenite phase at stresses that are lower than the yield stress and (2) the Magee effect, in which a crystallographically preferred martensite variant forms due to applied stress and leads to a macroscopic shape change [8]. These effects have been theoretically studied using micromechanical models [4,9] which have led to improved understanding of the phenomena. The interaction of martensitic transformations and plasticity has also been studied in the context of shape memory alloys [10] using Finite Element Method (FEM) models. However, such models do not consider the morphological aspects of the underlying martensitic transformation.

The martensitic transformation in steel can result in the formation of 24 equivalent variants. The complex morphology can significantly influence the effective mechanical behavior. Thus, there is a need for models that study transformation-induced plasticity, taking into account the complex martensite domain patterns that are observed in steel. Over the last two decades, phase field models have been successful in simulating the complex martensitic microstructure [11–16]. Plastic effects have also been considered by using discrete dislocation dynamics as well as continuum plasticity [17–20]. In the context of steel, phase field models with elastic and plastic effects have been extensively used to study the martensite patterns [21,22].

In the present work, the role of transformation plasticity in steel is studied using the phase field approach with a focus on temperature-induced transformations as well as stress-induced transformation. The advantage of using the phase field model is that both the Greenwood-Johnson mechanism and the Magee mechanism can be studied within a

---

*Corresponding author: rajeev@ihpc.a-star.edu.sg

103607-1

unified framework. The aim of this study is to exploit capabilities of the phase field approach to shed light on how plasticity due to martensitic transformations influences the martensite morphology as well as the mechanical behavior over a range of temperatures. Barring a recent work on lath martensite [23], the phase field studies have used the Bain orientation relationship [24] with only three crystallographic variants to simulate the martensitic domain patterns. It is well known that the commonly observed orientational relationships in steel are the Nishiyama-Wassermann (NW; 12 crystallographically equivalent variants) [25] and Kurdjumov-Sachs (KS; 24 crystallographically equivalent variants) [26]. Therefore, in the present model, all 24 variants associated with the KS orientational relationship are considered (the transformation strains are obtained in terms of the lattice parameters for a 1 wt% steel). Since a temperature-dependent driving force is considered, a temperature-dependent plasticity is also incorporated using the methodology developed by Guo *et al.* [18]. Temperature-dependent flow curves with isotropic plasticity for AISI 52100 (a steel composition with carbon concentration close to 1 wt%) are used to study the role of plasticity [27]. To study temperature-induced martensitic transformations, quenches from the austenite phase to a range of temperatures below the T_0 temperature (temperature where austenite and martensite have same free energy) are considered. Deformation-induced transformations are studied for a range of temperatures between T_0 and M_s (martensitic start temperatures). To isolate the role of transformation plasticity, some cases without plastic effects for both temperature-induced and stress-induced transformations are also studied.

II. PHASE FIELD MODEL

The martensitic transformation is described by a multiple-order-parameter phase field model. The variants of the martensite phase are described by a vector order parameter $\vec{\eta}$ with components η_i such that the mth variant is represented by $\eta_i = \eta_m \neq 0$ and $\eta_i = 0$ for $i \neq m$. The components η_m ($m = 1, \ldots, 24$) describe the 24 variants of the martensite phase. The parent austenite is described by the case when all components of the order parameter vanish, i.e., $\eta_m = 0$ for $m = 1, \ldots, 24$. The free energy considered in this work is given as

$$\mathcal{F} = \int_V dV (f_{\text{chem}} + f_{el}), \tag{1}$$

where f_{chem} is the free energy density describing the martensitic transformation and f_{el} represents the elastic strain energy density associated with the transformation. The free energy density f_{chem} is expressed in terms of the order parameter components as

$$f_{\text{chem}} = G_0 \left[\tau \left(\sum_{i=1}^{24} \eta_i^2 \right) - 2 \left(\sum_{i=1}^{24} \eta_i^3 \right) + \left(\sum_{i=1}^{24} \eta_i^2 \right)^2 \right] + \sum_{i=1}^{24} \frac{K}{2} (\nabla \eta_i)^2, \tag{2}$$

where G_0 is the reference free energy density that is related to the driving force of the transformation and $\tau = (T - $

$T_c)/(T_0 - T_c)$ is a temperature-dependent coefficient. Here T_0 is the temperature at which the austenite and martensite have the same free energy ($\tau = 1$), and T_c is a temperature at which the martensite phase becomes unstable ($\tau = 0$). Here, the spatially homogeneous part of Eq. (2) describes a function with 25 minima corresponding to 24 martensitic variants and one austenitic well. This choice of the free energy has been shown to describe thermomechanical behavior of martensites [28]. Since martensitic transformations in steel are associated with a large shape and/or volume change, the growth of martensitic nuclei may lead to enormous elastic energy. The local stresses can be so large that localized plastic deformation may be induced. Thus, both elastic and plastic deformations need to be incorporated in the phase field model. The elastic contribution to the free energy is expressed as

$$f_{el} = \frac{C_{11}}{2} \left(e_{xx}^2 + e_{yy}^2 + e_{zz}^2 \right) + C_{12} (e_{xx} e_{yy} + e_{xx} e_{zz} + e_{yy} e_{zz}) + 2C_{44} \left(e_{xy}^2 + e_{yz}^2 + e_{xz}^2 \right), \tag{3}$$

where

$$e_{ij} = \varepsilon_{ij} - \sum_{m=1}^{24} H(\eta_m) \varepsilon_{ij}^{KS,m} - \varepsilon_{ij}^p. \tag{4}$$

Here, $\varepsilon_{ij} = \frac{1}{2}[\partial u_i/\partial x_j + \partial u_j/\partial x_i]$ is the infinitesimal strain tensor calculated using the displacement variables u_i, $\varepsilon_{ij}^{KS,m}$ represents the transformation associated with the mth KS variant, and ε^p are the components of the plastic strain tensor. The function $H(\eta_m) = \eta_m^2$ is chosen. The constants C_{11}, C_{12}, and C_{44} are the elastic constants of cubic symmetry. For simplicity, the contribution that arises from differences in the hardening of austenite and martensite has been neglected. The details of calculation of the transformation strains $\varepsilon_{ij}^{KS,m}$ and the plastic strains ε^p are described below.

A. Transformation strain for the KS orientation relationship

In this section, the transformation strains obeying the Kurdjumov-Sachs relationship are described [26]. According to the KS relationship, a typical martensite variant satisfies the conditions

$$(111)_A \parallel (011)_M \quad [10\bar{1}]_A \parallel [11\bar{1}]_M. \tag{5}$$

By symmetry, 24 such equivalent variants can be formed. In order to compute the transformation strains for all variants, the deformation gradient is first defined as

$$F_{ij} = \delta_{ij} + \frac{\partial u_i}{\partial x_j}, \tag{6}$$

where u_i represents the displacement field, x_i is the material coordinate, and δ_{ij} is the Kronecker delta. To derive the deformation gradient for the KS orientation relationship, the strain-based approach proposed by Koumatos and Muehlemann [29] is adopted. To begin with, the deformations for the

simple Bain strain [24] are defined as

$$\boldsymbol{B}_1 = \begin{bmatrix} \beta & 0 & 0 \\ 0 & \alpha & 0 \\ 0 & 0 & \alpha \end{bmatrix}, \quad \boldsymbol{B}_2 = \begin{bmatrix} \alpha & 0 & 0 \\ 0 & \beta & 0 \\ 0 & 0 & \alpha \end{bmatrix},$$

$$\boldsymbol{B}_3 = \begin{bmatrix} \alpha & 0 & 0 \\ 0 & \alpha & 0 \\ 0 & 0 & \beta \end{bmatrix}, \tag{7}$$

where $\alpha = \frac{\sqrt{2}a}{a_0}$ and $\beta = \frac{c}{a_0}$ are calculated from the lattice parameters of the cubic phase (a_0) and the tetragonal martensite phase (a, c). The overall deformation can be decomposed into stretch due to Bain strain and rigid-body rotation, giving the desired orientation relationship. For the KS relationship, the deformation associated with the first KS variant is expressed as

$$T_{ij}^{KS,1}(r) = R_{im}[\theta(r), [111]_A]R_{mn}[\theta(r), [\bar{1}10]_A]B_{3_{nj}}, \tag{8}$$

where r is the ratio of tetragonality ($r = \frac{c}{a}$) and $\boldsymbol{R}[\theta, \boldsymbol{o}]$ denotes a rotation matrix describing a counterclockwise rotation by an angle θ about a vector $\boldsymbol{o}$. The angles θ and ϕ in the rotation matrices can be identified as [29]

$$\theta(r) = \arccos\left(\frac{\sqrt{3}\sqrt{r^2+1}+1}{2\sqrt{r^2+2}}\right),$$

$$\phi(r) = \arccos\left(\frac{1+\sqrt{2}r}{\sqrt{3}\sqrt{1+r^2}}\right). \tag{9}$$

The deformation gradients associated with the remaining KS variants $T_{ij}^{KS,m}$ are calculated by applying the group of rotations $\mathcal{P}^{24}$ that maps a cube to itself:

$$F_{ij}^{KS,m} = P_{ik}(m)T_{kl}^{KS,1}(r)P_{lj}(m). \tag{10}$$

Assuming the geometrically linear theory, the transformation strain is calculated as

$$\varepsilon_{ij}^{KS,m}(r) = \frac{1}{2}\left(F_{ij}^{KS,m}(r) + F_{ji}^{KS,m}(r)\right) - \delta_{ij}. \tag{11}$$

The advantage of this approach is that the transformation strains now explicitly depend on the tetragonality ratio r.

B. Plasticity model

The evolution of plastic strain is computed within the theory of phenomenological rate-independent plasticity with the associated flow rule that distinguishes between the yield stress of the austenite σ_y^A and the yield stress of the martensite σ_y^M. The model proposed by Guo *et al.* [18] is used here for its computational efficiency in connection with phase field models [21,30]. The evolution equation for the plastic strain $\boldsymbol{\varepsilon}^p$ presented by [18] is derived from minimizing the shear strain energy density W^{shear} by solving

$$\frac{\partial \varepsilon_{ij}^p(\boldsymbol{x}_p, t)}{\partial t} = -k_{ijkl}\frac{\delta W^{\text{shear}}}{\delta \varepsilon_{kl}^p(\boldsymbol{x}_p, t)}, \tag{12}$$

where $\boldsymbol{x}_p$ is the yielding region. The shear strain energy is defined as

$$W^{\text{shear}} = \frac{1}{2}e_{ij}^{dev}C_{ijkl}e_{kl}^{dev}, \tag{13}$$

where the superscript *dev* refers to the deviatoric part of the strain tensor. Numerically, the equation is evolved only

in the region $\boldsymbol{x}_p$, where the consistency condition has been violated. We would also like to note that this is a homogenized plasticity model, and the authors [18] have shown that Eq. (12) can also be written in the more standard form known from the Prandtl-Reuss theory in which $d\varepsilon_{ij}^p = d\lambda\frac{\partial f}{\partial \sigma_{ij}}$.

In the present case of anisotropic (cubic) elasticity we assume that k_{ijkl} equals the compliance tensor $S_{ijkl} = [\tilde{C}_{ijkl}]^{-1}$, where the shear-related components in $\tilde{C}_{ijkl}$ are calculated as $\frac{C_{11}-C_{12}}{2}$, instead of C_{44} defined in C_{ijkl}. This is necessary in order to be consistent with the flow rule of the associated plasticity model. The equations of plastic strain [Eq. (12)] are evolved to satisfy the yielding condition $f(\boldsymbol{\sigma}) = 0$, where the plastic potential $f(\boldsymbol{\sigma})$ is defined of a von Mises material as

$$f(\sigma_{ij})$$
$$= \sqrt{\frac{3}{2}}\sqrt{\sigma_{ij} : \sigma_{ij}} - \left\{\sigma_y^A + \left[\sigma_y^M - \sigma_y^A\right]g(\eta_i) + h(\eta_i, \hat{\varepsilon}^p)\right\}, \tag{14}$$

where σ_y^A and σ_y^M are the initial yield stresses of the austenite and martensite phases, g is a step function to distinguish between the phases (austenite for $g = 0$ and martensite for $g = 1$), and h is the hardening modulus function of the equivalent plastic strain $\hat{\varepsilon}^p$. The function that distinguishes between the yield stress of martensite and austenite is defined as

$$g(\eta_i) = \begin{cases} 1 & \text{if} \quad \sum_{i=1}^{24}\eta_i > 0.5, \\ 0 & \text{if} \quad \sum_{i=1}^{24}\eta_i \leqslant 0.5. \end{cases} \tag{15}$$

Further, the model accounts for the isotropic hardening defined by the following power-law functions:

$$h(\eta_i, \hat{\varepsilon}^p) = \begin{cases} C_1^M(\hat{\varepsilon}^p)^{C_2^M} & \text{if} \quad \sum_{i=1}^{24}\eta_i > 0.5, \\ C_1^A(\hat{\varepsilon}^p)^{C_2^A} & \text{if} \quad \sum_{i=1}^{24}\eta_i \leqslant 0.5, \end{cases} \tag{16}$$

where the constants C_1 and C_2 are defined for both the martensite and austenite phases. These constants are temperature dependent and are presented in Eq. (19).

The equivalent plastic strain is calculated as the accumulation of equivalent plastic strain increments:

$$\hat{\varepsilon}^p = \int_0^t d\hat{\varepsilon}^p dt, \quad d\hat{\varepsilon}^p = \sqrt{\frac{2}{3}d\varepsilon_{ij}^p d\varepsilon_{ij}^p}. \tag{17}$$

The numerical implementation of the plasticity equations is similar to the standard radial-return algorithm. Beginning with a trial stress $\boldsymbol{\sigma}^{tr}$, if the stress point is found to lie outside of the yield surface (here defined by the domain $\boldsymbol{x}_p$), the amount of plastic strain is calculated to push the stress point back onto the yield surface. The directions of the plastic strain tensor components are given by Eq. (12), and the equation is evolved sufficiently long with a relatively small time step Δt until Eq. (14), $f(\boldsymbol{\sigma}) = 0$, is satisfied. This is a process similar to finding $\Delta\lambda$ in the radial return algorithm. The consistency is ensured at each loading increment of each time step of the phase field simulation.

TABLE I. Transformation strains.

B_1			B_2			B_3		
$\varepsilon^{KS,2} = \begin{bmatrix} -0.182 & -0.005 & -0.023 \\ -0.005 & 0.116 & -0.005 \\ -0.023 & -0.005 & 0.106 \end{bmatrix}$			$\varepsilon^{KS,4} = \begin{bmatrix} 0.106 & -0.023 & -0.005 \\ -0.023 & -0.182 & -0.005 \\ -0.005 & -0.005 & 0.116 \end{bmatrix}$			$\varepsilon^{KS,1} = \begin{bmatrix} 0.106 & -0.005 & -0.023 \\ -0.005 & 0.116 & -0.005 \\ -0.023 & -0.005 & -0.182 \end{bmatrix}$		
$\varepsilon^{KS,3} = \begin{bmatrix} -0.182 & -0.023 & -0.005 \\ -0.023 & 0.106 & -0.005 \\ -0.005 & -0.005 & 0.116 \end{bmatrix}$			$\varepsilon^{KS,5} = \begin{bmatrix} 0.116 & -0.005 & -0.005 \\ -0.005 & -0.182 & -0.023 \\ -0.005 & -0.023 & 0.106 \end{bmatrix}$			$\varepsilon^{KS,6} = \begin{bmatrix} 0.116 & -0.005 & -0.005 \\ -0.005 & 0.106 & -0.023 \\ -0.005 & -0.023 & -0.182 \end{bmatrix}$		
$\varepsilon^{KS,7} = \begin{bmatrix} -0.182 & 0.005 & 0.023 \\ 0.005 & 0.116 & -0.005 \\ 0.023 & -0.005 & 0.106 \end{bmatrix}$			$\varepsilon^{KS,9} = \begin{bmatrix} 0.106 & 0.023 & 0.005 \\ 0.023 & -0.182 & -0.005 \\ 0.005 & -0.005 & -0.116 \end{bmatrix}$			$\varepsilon^{KS,8} = \begin{bmatrix} 0.106 & 0.005 & 0.023 \\ 0.005 & 0.116 & -0.005 \\ 0.023 & -0.005 & -0.182 \end{bmatrix}$		
$\varepsilon^{KS,10} = \begin{bmatrix} -0.182 & 0.023 & 0.005 \\ 0.023 & 0.106 & -0.005 \\ 0.005 & -0.005 & 0.116 \end{bmatrix}$			$\varepsilon^{KS,12} = \begin{bmatrix} 0.116 & 0.005 & 0.005 \\ 0.005 & -0.182 & -0.023 \\ 0.005 & -0.023 & 0.106 \end{bmatrix}$			$\varepsilon^{KS,11} = \begin{bmatrix} 0.116 & 0.005 & 0.005 \\ 0.005 & 0.106 & -0.023 \\ 0.005 & -0.023 & -0.182 \end{bmatrix}$		
$\varepsilon^{KS,13} = \begin{bmatrix} -0.182 & 0.005 & -0.023 \\ 0.005 & 0.116 & 0.005 \\ -0.023 & 0.005 & 0.106 \end{bmatrix}$			$\varepsilon^{KS,15} = \begin{bmatrix} 0.106 & 0.023 & -0.005 \\ 0.023 & -0.182 & 0.005 \\ -0.005 & 0.005 & 0.116 \end{bmatrix}$			$\varepsilon^{KS,14} = \begin{bmatrix} 0.106 & 0.005 & -0.023 \\ 0.005 & 0.116 & 0.005 \\ -0.023 & 0.005 & -0.182 \end{bmatrix}$		
$\varepsilon^{KS,16} = \begin{bmatrix} -0.182 & 0.023 & -0.005 \\ 0.023 & 0.106 & 0.005 \\ -0.005 & 0.005 & 0.116 \end{bmatrix}$			$\varepsilon^{KS,18} = \begin{bmatrix} 0.116 & 0.005 & -0.005 \\ 0.005 & -0.182 & 0.023 \\ -0.005 & 0.023 & 0.106 \end{bmatrix}$			$\varepsilon^{KS,17} = \begin{bmatrix} 0.116 & 0.005 & -0.005 \\ 0.005 & 0.0106 & 0.023 \\ -0.005 & 0.023 & -0.182 \end{bmatrix}$		
$\varepsilon^{KS,19} = \begin{bmatrix} -0.182 & -0.005 & 0.023 \\ -0.005 & 0.116 & 0.005 \\ 0.023 & 0.005 & 0.106 \end{bmatrix}$			$\varepsilon^{KS,21} = \begin{bmatrix} 0.106 & -0.023 & 0.005 \\ -0.023 & -0.182 & 0.005 \\ 0.005 & 0.005 & 0.116 \end{bmatrix}$			$\varepsilon^{KS,20} = \begin{bmatrix} 0.106 & -0.005 & 0.023 \\ -0.005 & 0.116 & 0.005 \\ 0.023 & 0.005 & -0.182 \end{bmatrix}$		
$\varepsilon^{KS,22} = \begin{bmatrix} -0.182 & -0.023 & 0.005 \\ -0.023 & 0.106 & 0.005 \\ 0.005 & 0.005 & 0.116 \end{bmatrix}$			$\varepsilon^{KS,24} = \begin{bmatrix} 0.116 & -0.005 & 0.005 \\ -0.005 & -0.182 & 0.023 \\ 0.005 & 0.023 & 0.106 \end{bmatrix}$			$\varepsilon^{KS,23} = \begin{bmatrix} 0.116 & -0.005 & 0.005 \\ -0.005 & 0.106 & 0.023 \\ 0.005 & 0.023 & -0.182 \end{bmatrix}$		

C. Equations of motion

The kinetics of the martensitic transformation is simulated using the phase field dynamical equations

$$-\frac{1}{\Gamma}\frac{\partial \eta_i}{\partial t} = \frac{\delta \mathcal{F}}{\delta \eta_i} = G_0\left[2\tau\eta_i - 6\eta_i^2 + 4\eta_i\left(\sum_{j=1}^{24}\eta_j^2\right)\right]$$
$$- K\nabla^2\eta_i + \frac{\delta f_{el}}{\delta \eta_i}, \qquad (18)$$

which is solved together with enforcing the mechanical equilibrium $\frac{\partial \sigma_{ij}}{\partial x_j} = 0$, $\sigma_{ij} = \frac{\partial f_{el}}{\partial \varepsilon_{ij}}$ at each numerical time step. Here, Γ is a kinetic coefficient related to the mobility of the interface. For computational convenience, dimensionless time and space variables are introduced as $\vec{r} = \delta \vec{r}'$ and $t = t^* t'$, where $t^* = 1/(\Gamma G_0)$ is the characteristic timescale of the simulations and δ is the smallest length scale in the simulation. Similarly, a rescaled gradient coefficient is introduced as $K' = K/\delta^2 G_0$. Since reliable data for the kinetic coefficient Γ are not available, all timescales are measured in units of t^*.

D. Material parameters

A high-carbon steel (AISI 52100) is used as an example in the present simulations. The chemical driving force in Eq. (2) is specified by choosing the reference free energy $G_0 = 3000$ J/mol and the equilibrium temperature

$T_0 = 723$ K, which is the typical value for steel with 1 wt% carbon [31]. The temperature T_c is regarded as an adjustable parameter. The value of $T_c = 315$ K is chosen such that the fraction of martensite at room temperature during the temperature-induced transformation is close to the experimentally observed value for AISI 52100 (see Sec. III). The gradient coefficient is chosen to be $K = 0.106 \times 10^{-10}$ J/m [32], and the grid spacing is 1 nm. The transformation strains in Eq. (11) are calculated for a steel with 1 wt% carbon with the lattice parameters $a_0 = 0.36$ nm, $a = 0.285$ nm, $c = 0.298$ nm [31]. Table I shows the transformation strain matrices for all 24 variants obtained using the above lattice constants. Figure 12 in the Appendix illustrates the corresponding unit cell deformations associated with each of the 24 variants. The elastic constants used in the simulations are $C_{11} = 209$ GPa, $C_{12} = 133$ GPa, and $C_{44} = 121$ GPa [21]. To incorporate plastic effects, temperature-dependent power laws [see Eq. (16)] for AISI 52100 are adopted from Ref. [27], and the coefficients C_1^A, C_1^M and C_2^A, C_2^M for the austenite and martensite phases are given as

$$C_1^M = 4.35 \times 10^3 - 4.11T,$$
$$C_2^M = 7.97 \times 10^{-3} + 1.27 \times 10^{-4}T,$$
$$C_1^A = 1.06 \times 10^3 - 1.09T,$$
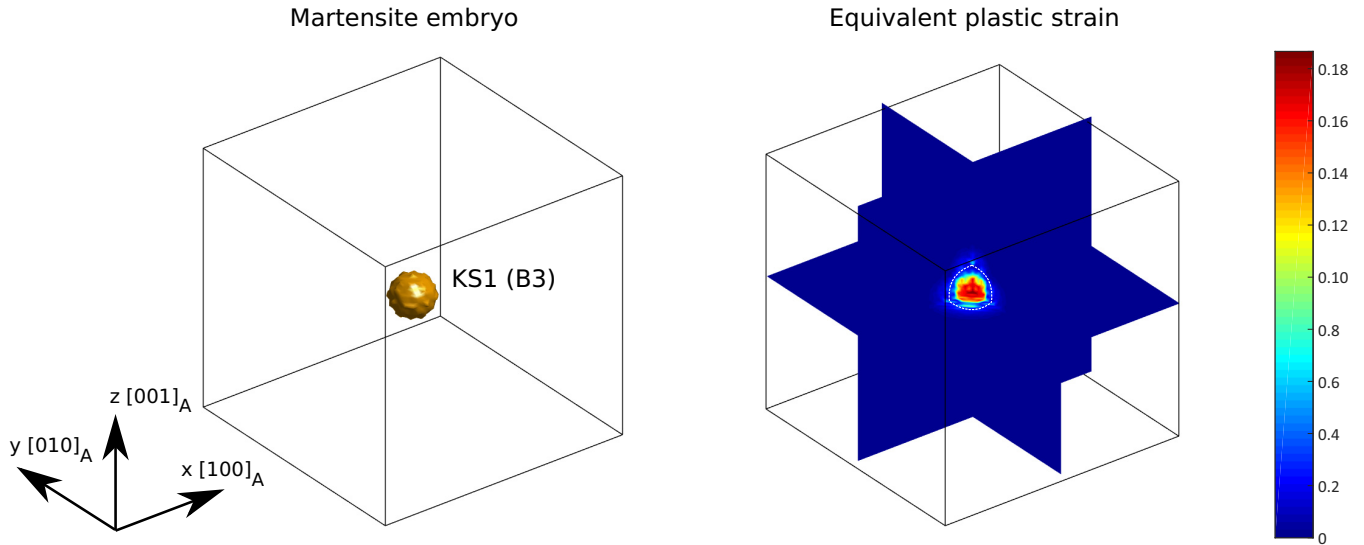$$C_2^A = 1.22 \times 10^{-1} + 3.88 \times 10^{-5}T, \qquad (19)$$

FIG. 1. Martensite embryo at $T = 623$ K (left) and equivalent plastic strain $\hat{\varepsilon}^p$ (right) on three mutually perpendicular planes passing through the center. The box shows the shape of the initial untransformed austenite (with dimensions $64 \times 64 \times 64$ nm^3).

where C_1^M and C_1^A are given in megapascals. The initial yield stresses are calculated from Eq. (16) assuming $\hat{\varepsilon}^p = 0.00005$ [27] and are therefore also temperature dependent. The initial yield stress of austenite varies between 283 MPa at $T = 350$ K and 253 MPa at $T = 422$ K. Similarly, the initial yield stress of martensite varies between 3383 MPa at $T = 350$ K and 2863 MPa at $T = 422$ K.

III. SIMULATION OF TEMPERATURE-INDUCED TRANSFORMATIONS

Starting from an initial austenite phase, quenches to different temperatures below T_0 are simulated using the model described in Sec. II. The representative volume element is subjected to periodic boundary conditions. Note that the periodicity of the displacement variables implies that $\langle \varepsilon_{ij} \rangle = 0$. The mechanically constrained condition has been imposed to model a single grain, deep inside a polycrystal. Such a grain cannot be stress free as it will be mechanically constrained by the surrounding grains. The initial austenite phase is set up by setting all order components to zero, except in a spherical region of radius 5δ, $\delta = 1$ nm, at the center of the simulation cell where $\eta_1 = 1$. This represents an initial embryo of the martensite corresponding to KS1 (B3).

Figure 1 shows the initial martensite embryo (left) and the associated equivalent plastic strain (right) at $T = 623$ K for the case when plasticity is incorporated. It is clear that plastic deformations occurred inside the embryo (martensite) as well as in its surroundings (austenite). This plastic deformation relaxes the elastic energy that arises from the misfit between the austenite and martensite.

Interestingly, the simulation result shows that the initial martensitic embryo in this case remains stable and does not further evolve. However, an analogous simulation performed at the same temperature but assuming purely elastic conditions (both martensite and austenite) showed that the

initial embryo shrank. Therefore, the stabilization of the martensite in the elastoplastic case can be attributed to the transformation-induced plasticity.

The temperature-induced transformation for the same elastoplastic problem simulated at lower quenching temperatures is depicted in Figs. 2 and 3. Figure 2 shows the fraction of martensite as a function of the rescaled time for different temperatures, and Fig. 3 shows the associated equilibrium martensitic patterns. The transformed fraction is calculated by counting the fraction of spatial points for which any one of the order parameter components is larger than 0.2. In Fig. 3,
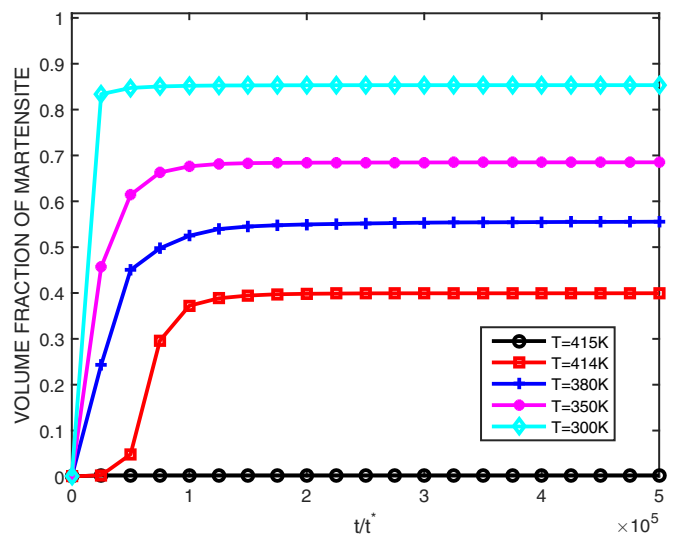

FIG. 2. The transformed fraction of the martensite for the case with plasticity as a function of time for different temperatures. The volume fraction of martensite increases with decreasing quenching temperature.
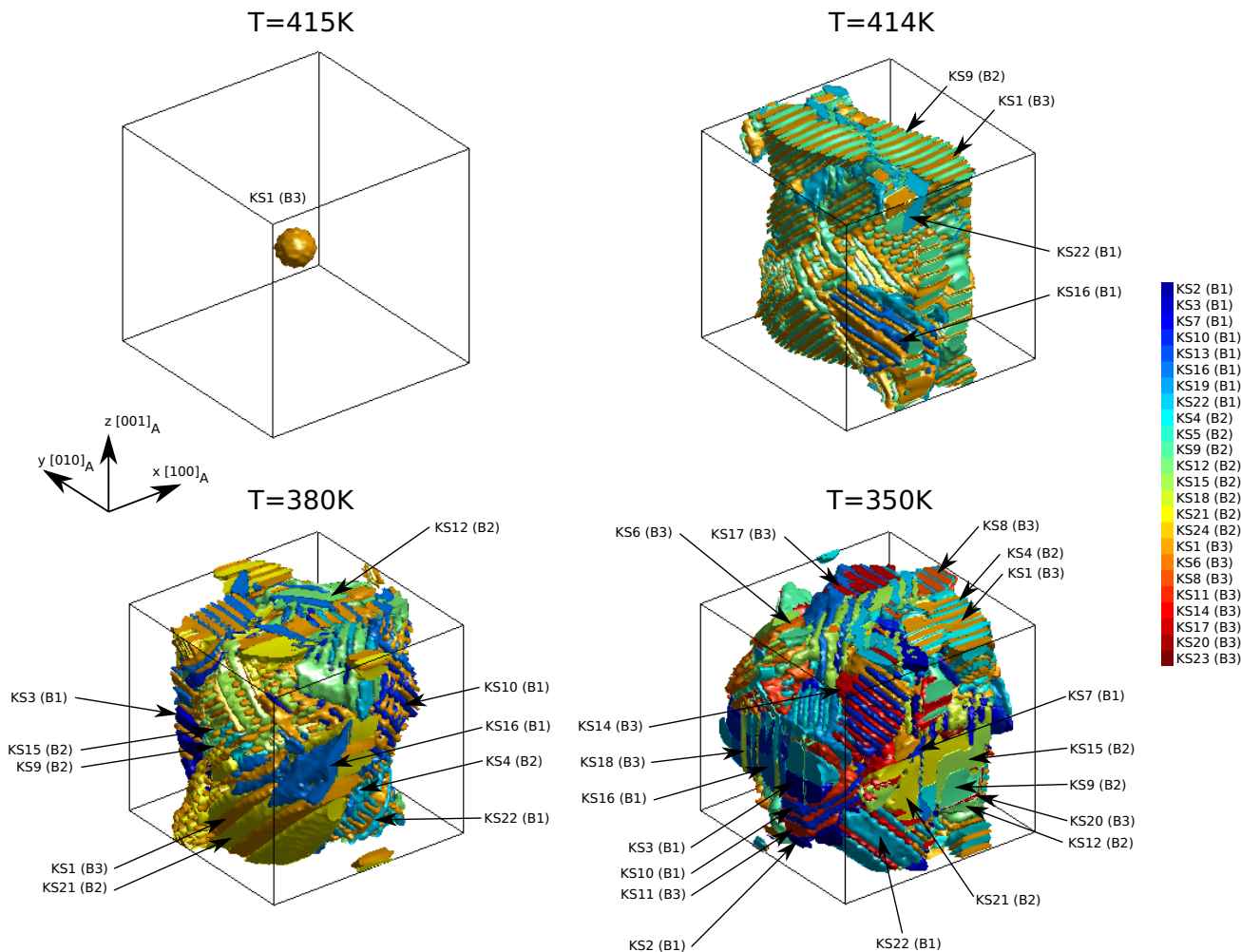
FIG. 3. Simulated martensite domain patterns at different temperatures. The box shows the shape of the initial untransformed austenite. The volume fraction and the complexity of the martensite increase with decreasing temperature (with dimensions $64 \times 64 \times 64$ nm^3).

each color corresponds to one of the 24 variants, and the empty regions represent the austenite phase. The color map is labeled such that the KS variants belonging to the same Bain group share a similar color (B1, blue; B2, green; B3, red). The martensite start temperature M_s for the model is calculated to be $T = 414$ K, above which the martensitic embryo does not grow. While at lower temperatures the embryo evolves into a microstructure of finely twinned martensitic variants, it is clear that the entire domain does not fully transform into martensite. The amount of martensite increases as the temperature decreases, and at room temperature, the fraction of transformed austenite is about 85%, which is close to the experimental value of bulk AISI52100 [27]. (As discussed earlier, the free energy parameters, mainly G_0 and T_c, were adjusted to obtain this value of the transformed fraction).

Analyzing Fig. 3, we notice that the critical temperature for embryo growth is $T = 414$ K. At the temperature $T = 415$ K, the initial defect does not grow. Although a localized yielding similar to that in Fig. 1 relaxes the elastic energy, the driving force is still not sufficient to cause growth of the transformation. At $T = 414$ K, the driving force is large

enough, and the formation of internally twinned martensite plates in austenite matrix is observed. However, it is clear that the entire simulation domain does not transform and retained austenite is observed. At lower temperatures, the fraction of martensite increases. It can be further observed that at higher temperatures, only some of the variants are formed after the transformation; at lower temperatures (e.g., $T = 350$ K), almost all 24 variants are formed.

In order to understand the role played by plasticity, the transformation case at $T = 414$ K is analyzed by comparing the martensitic domain pattern (Fig. 4, left) with the corresponding equivalent plastic strain distribution (Fig. 4, right). Plastic strains are observed within the martensite as well as in the surrounding austenite. The plastic deformation of the austenite is akin to the Greenwood-Johnson mechanism where the weaker austenite undergoes plastic deformation to accommodate the shape change due to martensitic transformation. As the martensite domain grows, it also inherits the preexisting plastic deformation of the austenite. This was found in earlier works [33,34]. Note that there are additional plastic strains at the twin boundaries. These arise due to shear stresses
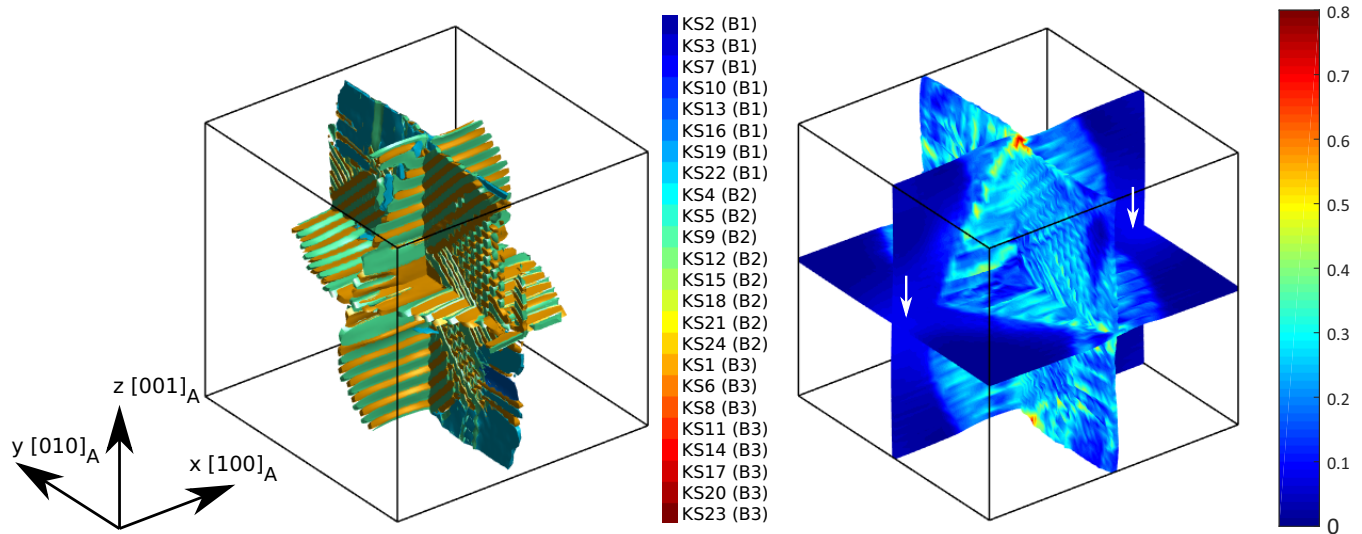
FIG. 4. Martensite domain pattern at $T = 414$ K (left) and equivalent plastic strain $\hat{\varepsilon}^p$ (right) on three mutually perpendicular planes passing through the center of the simulation box. The white arrows in the right panel indicate regions of the austenite that have undergone plastic deformation (with dimensions $64 \times 64 \times 64$ nm^3). The interfacial width of austenite-martensite interfaces is about 4–5 nm, whereas that for martensite-martensite interfaces is about 1–2 nm.

that exist at the diffuse twin interface [35,36]. Figure 4 clearly shows that the plastic deformation provides an additional mechanism to accommodate the phase transformation.

In order to isolate the role of plasticity, analogous simulations without incorporating plastic effects were performed under conditions identical to those in the case with plasticity. Quenches to several temperatures were considered. As discussed earlier, for the case without plasticity, it is found that at high temperatures, the initial defect is not stable and shrinks. For this case, at lower temperatures ($T < 412$ K), the driving force is sufficiently large to transform the incompatible spherical embryo into a region of fine twins so that the initial defect survives and leads to the growth of the martensite domains. Figure 5 shows the time evolution of the transformed fraction for the case without plasticity for different temperatures. It is interesting to note that no retained austenite is observed at any temperature for this case.

Figure 6 shows the martensite patterns at two temperatures. In contrast to the elastoplastic case in Fig. 3, no retained austenite is found in this case. Also, it is noticeable that the twins are finer in this case. Furthermore, a large number of variants are observed, even at higher temperatures. This should be contrasted with the plastic case, where fewer variants appeared at the same temperatures.

Figures 1–6 describe the transformation for a mechanically constrained system. However, it is known that the observed martensite patterns can be quite different for the stress-free case where a macroscopic shape change is allowed. For example, simulations by Yeddu *et al.* [21] showed that a single domain state with only one variant is formed for the stress-free case, whereas multiple variants formed for the constrained case. In order to understand the role played by the mechanical boundary conditions, we also simulated the transformation in the stress-free case for both the plastic and purely elastic cases, just below their respective martensite start temperatures. The stress-free case

was implemented by defining a strain tensor $\varepsilon_{ij} = \frac{1}{2}(\partial u_i/\partial x_j + \partial u_j/\partial x_i) + \varepsilon^a_{ij}$, where the strains ε^a_{ij} are chosen so that the average stress $\langle \sigma_{ij} \rangle = 0$. For both cases, the initial domain fully transformed to a macroscopically tetragonal state, which is in contrast to the constrained case in Fig. 3, where retained austenite is observed for the plastic case.

The differences in the morphology between the plastic and elastic cases can be understood in terms of the role played by transformation plasticity and the mechanical boundary conditions. As the martensite starts to grow, for a mechanically constrained system, for both elastic and plastic cases, it generates predominantly compressive strains in the surrounding austenite. The compressive strains are observed due to the
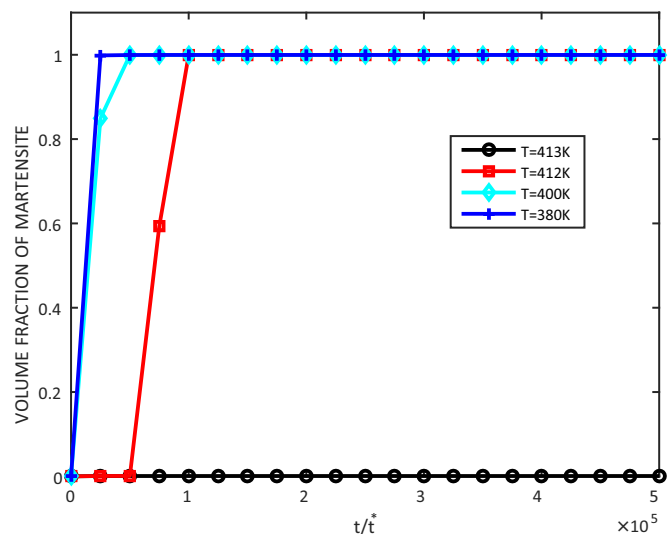

FIG. 5. The transformed fraction of the martensite for the case without plasticity as a function of rescaled time t^* for different temperatures.
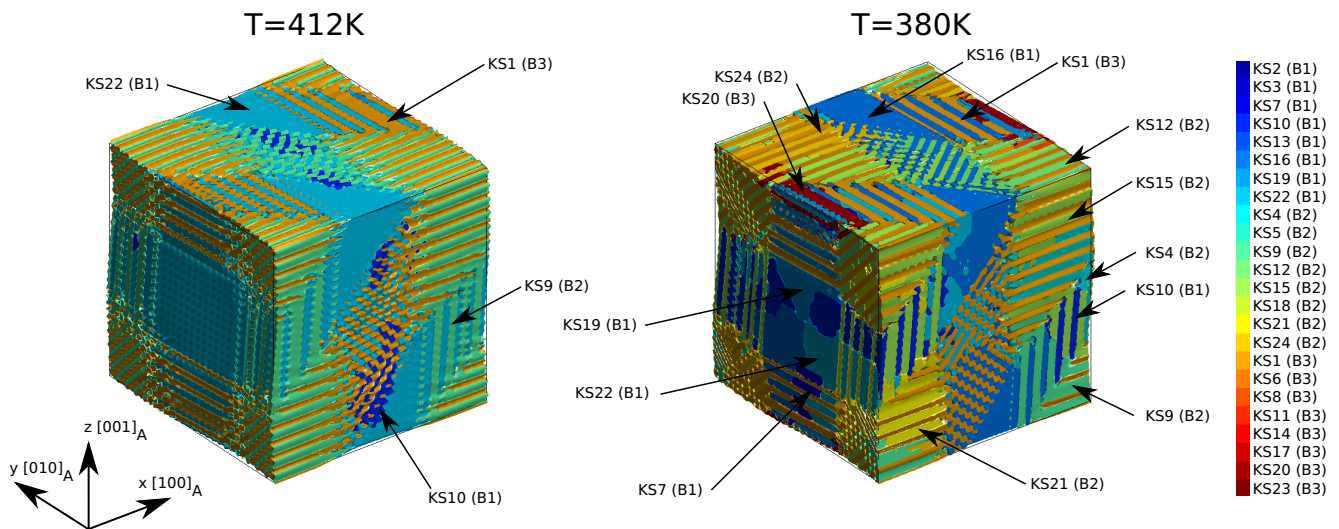
FIG. 6. Simulated martensite domain patterns for the case without plasticity at two different temperatures (for a system with dimensions $64 \times 64 \times 64$ nm^3).

fact that the martensite undergoes volume expansion and leads to a compression of the surrounding austenite as macroscopic shape change is not allowed. For the purely elastic case, the additional elastic energy due to compressed austenite can be overcome by forming a fine twinned pattern with a large number of variants, without any retained austenite (Fig. 6). As a result, there is no retained austenite. However, for the elastoplastic case, the plasticity induced in the austenite competes with the tendency to form a large number of variants to relieve the elastic energy. Therefore, the constraint of zero average strains is met by retaining the austenite that is compressed and plastically deformed. On the other hand, for the stress-free case, the volume change is accommodated by a macroscopic shape change, and the transformation is not suppressed, even for the case with plasticity.

These results clearly demonstrate the crucial role of the plastic deformation on the stability of retained austenite. It should be noted that the stability of austenite is crucial in the optimization of mechanical properties in steels that exhibit the TRIP effect, particularly to obtain both strength and ductility.

An important conclusion drawn from the above results is that plasticity plays a dual role during the transformation. On the one hand, in a mechanically constraint system (representing for instance a grain inside a polycrystalline system) the plasticity assists the nucleation by reducing the misfit strain energy, on the other hand it also facilitates the arrests of the transformation, thereby leading to the stability of the retained austenite.

IV. SIMULATIONS OF STRESS-INDUCED TRANSFORMATIONS

Martensitic phase transformation in steel may also be induced by an external deformation. This property is utilized in the so-called TRIP steels where a martensitic transformation occurs due to an external load at temperatures above M_s, where the driving force is not large enough to form

martensite without external deformation. There are two mechanisms of deformation-induced transformations [37]. If the transformation is stress induced, the applied stress provides an extra driving force for martensite formation. For plastic strain-induced transformations, plastic deformation leads to generation of additional nuclei that promote the martensitic transformation. In the present work, only stress-induced transformations are considered. To understand the mechanism of stress-induced transformations, an external stress is applied at temperatures where no martensitic transformation takes place without a stress, even if an embryo of the martensite exists in the initial austenite phase. The external stress is applied by defining a strain tensor $\varepsilon_{ij} = \frac{1}{2}(\partial u_i/\partial x_j + \partial u_j/\partial x_i) + \varepsilon_{ij}^a$, where the strains ε_{ij}^a are chosen so that the average stress can be fixed as $\langle \sigma_{ij} \rangle = \sigma_{ij}^a$. In the present work, a uniaxial deformation along the y direction is considered such that $\langle \sigma_{xx} \rangle = \langle \sigma_{xy} \rangle = \langle \sigma_{zz} \rangle = \langle \sigma_{yz} \rangle = \langle \sigma_{xz} \rangle = 0$ and $\langle \sigma_{yy} \rangle = \sigma_{yy}^a$, where σ_{yy}^a is the applied stress. Note that unlike the simulations in Sec. III, there is no mechanical constraint here, and an overall shape change in response to the applied stress is expected.

Similar to the case of temperature-induced transformation, a spherical embryo of the KS variant KS1 is placed in the austenite phase (see Fig. 1) at temperatures above the martensite start temperature of the model. The applied stress σ_{yy}^a is increased linearly with time. For comparison, identical simulations are run for the cases with and without plasticity. The maximum applied stress is $\sigma_{yy}^{\max} = 350$ MPa, and the stress is linearly increased for $t = 500000t^*$. Figure 7 shows the stress-strain curves for the two studied cases (with plasticity and without plasticity) at $T = 418$ K (the initial embryo is stable at this temperature for both cases, but no transformation is observed in the absence of applied stress).

After an initial linear elastic deformation, both cases transform to martensite at a critical stress. The externally applied stress decreases the austenite-martensite barrier and increases the driving force. This promotes the transformation to elastically favored variants. Thereafter, a linear elastic
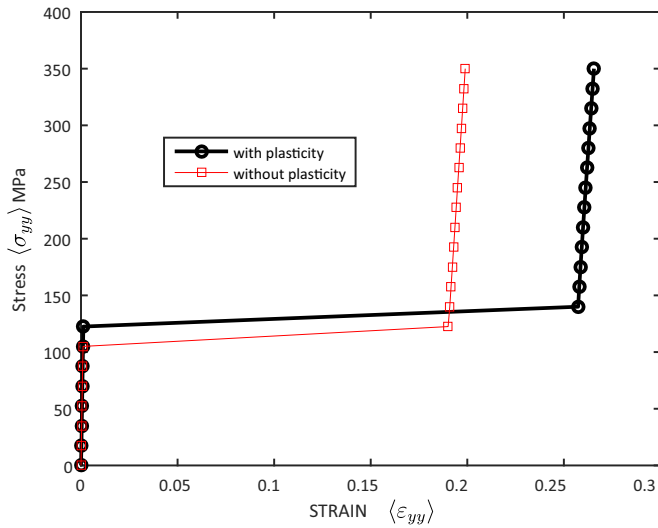
FIG. 7. Simulated stress strain curves for the plastic and nonplastic cases at $T = 418$ K.

deformation of martensite is observed. An important observation from Fig. 7 is that the uniaxial deformation at the end of the loading is significantly larger for the plastic case. To understand the role played by plasticity, it is instructive to examine the transformation strains and the plastic strains individually. The time evolution of the average strains during the loading process of Fig. 7 is shown in Fig. 8 for the case with plasticity as well as for the case without plasticity. Here, the average transformation and plastic strains are calculated as $\varepsilon_{ij}^{\text{trans}} = \langle \sum_{m=1}^{24} h(\eta_m) \varepsilon_{ij}^{KS,s} \rangle$ and $\varepsilon_{ij}^{pl} = \langle \varepsilon_{ij}^p \rangle$, respectively. It is clear by comparing Figs. 8(a) and 8(b) that transformation-induced plasticity significantly contributes to the total deformation. It should be remarked that the critical stress in Fig. 7 is much lower than the yield stress of the austenite at that temperature. Therefore, the plasticity is triggered by the phase transformation. This plastic strain arises

due to the deformation of the austenite caused by the growth of the martensite domain (similar to the Greenwood-Johnson mechanism). The stress generated in the austenite can be large enough to cause localized yielding. For the mechanically constrained case in Sec. III, this effect was responsible for arresting the transformation. For the case of uniaxial loading studied in this section, this effect leads to additional deformation since there is no mechanical constraint. The case without plasticity, on the other hand, is similar to the so-called Magee effect where stress-induced growth of favored variants is observed. Figures 7 and 8 also show that most of the stress-induced deformation is attributed to the phase transformation. However, the plastic strain generated due to the phase transformation is also significant and should not be neglected in an analysis of the mechanical behavior of steel.
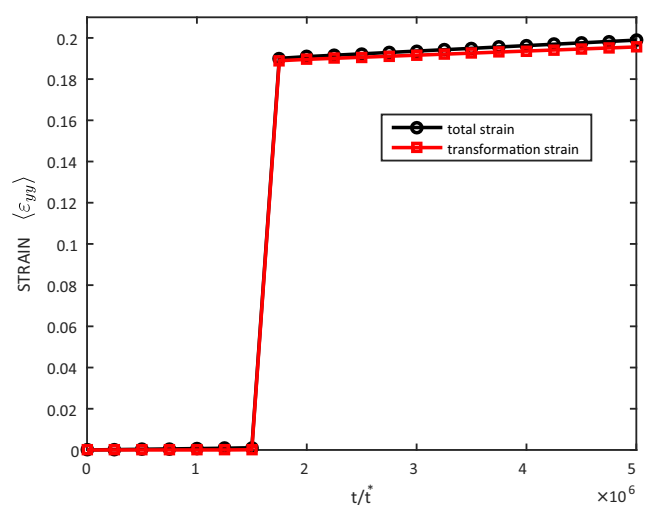
Figure 9 shows the martensite domain patterns at the end of the loading process for the cases shown in Fig. 7.

The variant KS1 was chosen as the initial embryo. From Table I, it is noted that this variant has its tetragonal axis along the y direction and is one of the favored variants when uniaxial stress σ_{yy} is applied. However, it is found that in addition to KS1, the variant KS10 is also formed for both cases. The two variants are formed to self-accommodate the shear stresses when a uniaxial stress is imposed. This should be contrasted with the case when only three variants corresponding to the pure Bain strains are considered. In that case, a single domain of the favored variant is expected to form. Figure 9 also demonstrates the influence of the plastic strain on the resulting pattern. For the case without plasticity, a fine twinned pattern of KS1 and KS10 is formed. For the plastic case, although KS1–KS10 twins are observed, the KS1 variant has a larger fraction. This is due to the fact that plastic deformation also contributes to accommodate the transformation in addition to the twin formation.

The competition between twinning and plasticity is further demonstrated by examining the stress-induced transformations at different temperatures. Figure 10 shows the final
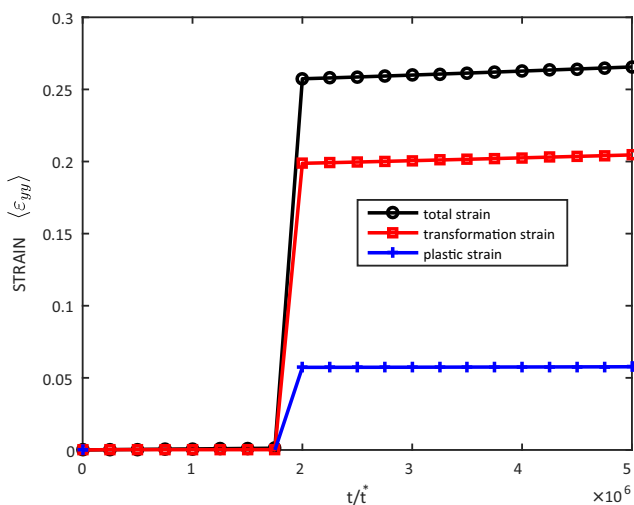
(a) With plasticity

(b) Without plasticity

FIG. 8. Time evolution of the average strains during the loading process shown in Fig. 7 for (a) the plastic and (b) nonplastic cases.
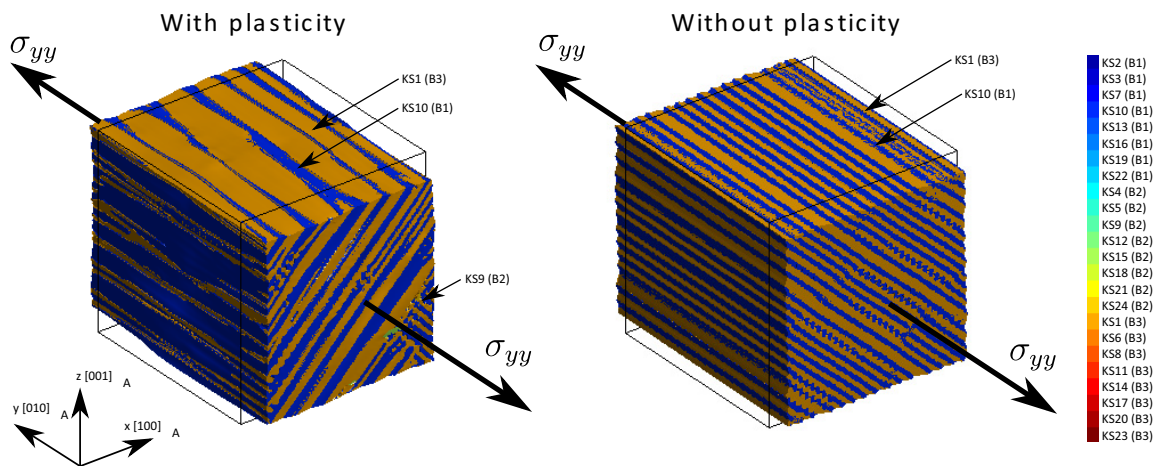
FIG. 9. Simulated martensite domain pattern at the maximum applied stress for the stress-strain curves in Fig. 7 at $T = 418$ K. The box shows the shape of the initial untransformed austenite (with dimensions $64 \times 64 \times 64$ nm^3).

patterns after stress-induced transformation at three temperatures. It is clear that the pattern for $T = 422$ K has a much higher fraction of KS1 compared to those at $T = 418$ K and $T = 420$ K. This manifests in a macroscopic shear that is visible for the $T = 422$ K case. In comparison, $T = 418$ K and $T = 420$ K appear macroscopically tetragonal.

Figure 11(a) shows the stress strain curves for the cases shown in Fig. 10.

The stress required to initiate the transformation increases with temperature. This is understood in terms of the decreasing driving force as temperature is increased. The macroscopic strain is also found to increase with temperature. In order to understand this, it is instructive to examine the development of the strains during the transformation. Figure 11(b) shows the time dependence of the transformations for three temperatures, and Fig. 11(c) shows the corresponding plastic strains. It is observed that the maximum transformation strain does not vary significantly with temperature. However, the induced plastic strains increase with temperature. This is due to the temperature-dependent plasticity model used in the present work. The increase in transformation-induced plastic strains at higher temperatures

explains the change in morphology observed in Fig. 10 for $T = 422$ K. The accommodation of the deformation by transformation plasticity leads to an increased tendency for formation of single variants.

V. SUMMARY AND DISCUSSION

A phase field study of the role of martensitic-transformation-induced plasticity in steels was presented. A phase field model incorporating elastic and plastic effects taking into account all 24 variants of the Kurdjumov-Sachs orientational relationship was used. The model was parameterized for a typical high-carbon steel (AISI 52100). Both temperature-induced and stress-induced martensitic transformations were studied. In order to understand the role of plastic effects, phase field simulations were run both with and without plastic effects.

For temperature-induced transformation in a mechanically constrained system, it is found that plasticity plays a dual role during the phase transformations. Localized plastic deformation relaxes the misfit strains associated with martensite embryos, helps to stabilize the embryos, and assists in the
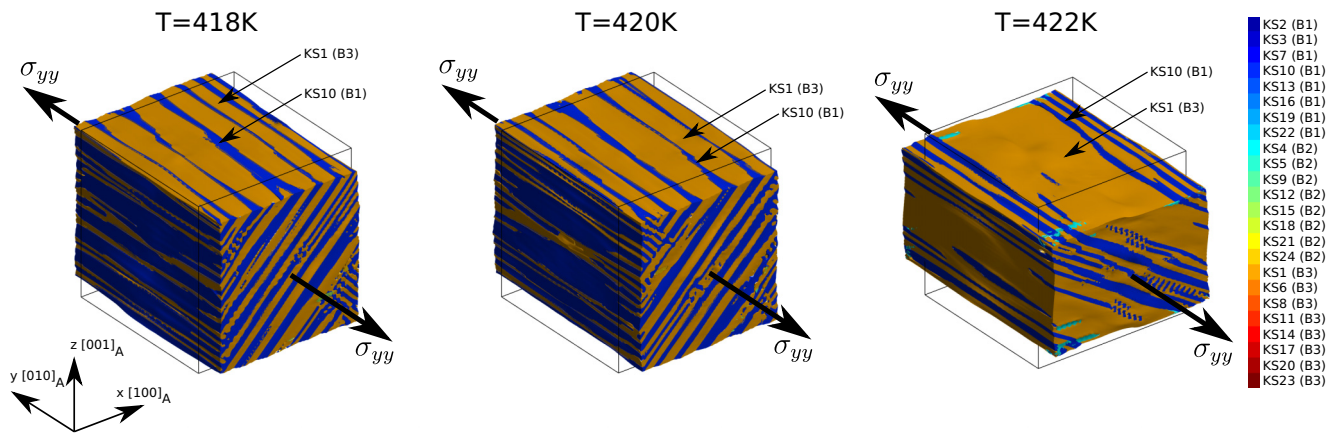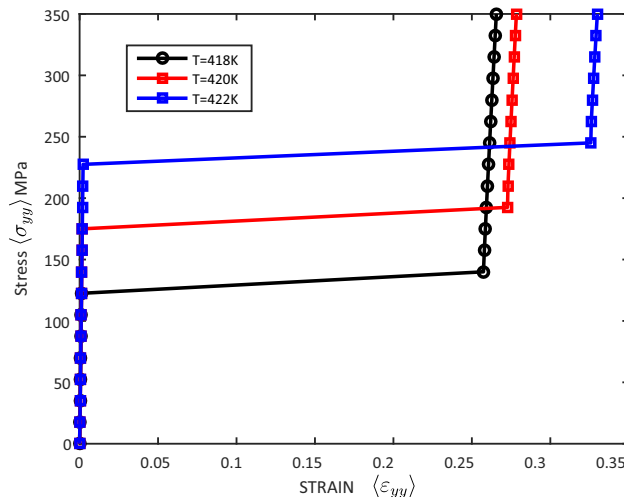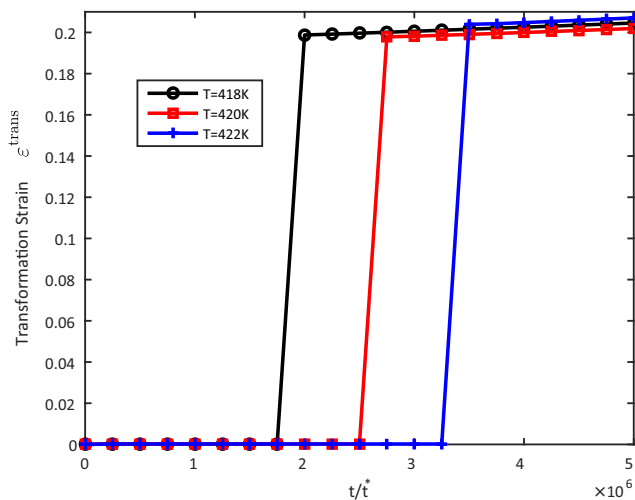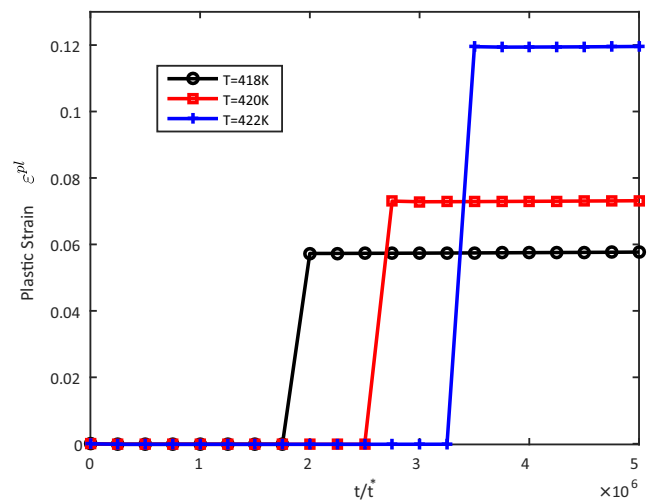

FIG. 10. Simulated martensite domain pattern at the maximum applied stress at three studied temperatures. The box shows the shape of the initial untransformed austenite (with dimensions $64 \times 64 \times 64$ nm^3).

(a) Corresponding stress-strain curves

(b) Average transformation strain

(c) Average plastic strain

FIG. 11. (a) The corresponding stress-strain curves of the cases in Fig. 10. The effect of temperature on (b) average transformation strain $\varepsilon_{ij}^{\text{trans}}$ and (c) average plastic strain ε_{ij}^{pl}. While the average transformation strain does not change much, the average plastic strain is significantly temperature dependent.

nucleation of the martensite. However, once the martensite starts to grow, the shape change associated with the martensite leads to plastic deformation of the surrounding austenite. For a mechanically constrained system, this plastic deformation competes with the tendency for nucleation and growth of multiple martensite variants for strain energy relief, therefore preventing further growth of martensite and stabilizing the retained austenite. On the other hand, when no plasticity is included, the entire system transforms to martensite for all temperatures below the martensite start temperature.

The martensitic transformation can also be induced by an external stress and can lead to formation of a favored martensite variant, depending on the loading direction. This leads to a macroscopic deformation caused by the shape change associated with the phase transformations. When plasticity is considered, the phase transformation is accompanied by a plastic deformation. Although the applied (macroscopic) stress is lower than the yield stress, plasticity is induced

due to the transformation. This is due to the fact that local shape change associated with the transformation can lead to stresses in the surrounding austenite that are large enough to trigger plastic deformation. The transformation-induced plasticity significantly enhances the overall stress-induced deformation. These observations are consistent with the classical mechanisms of transformation-induced plasticity [7,8]. Phase field simulations can be used to study the relative contributions of the two mechanisms. The simulations show that although most of the stress-induced deformation is attributed to the phase transformation, additional strain produced due to transformation plasticity is also significant and influences the martensite microstructure, particularly at high temperatures.

Some limitations of the model must be pointed out. The use of small-strain theory in the elasticity calculations is a source of inaccuracy, particularly for cases where large macroscopic strains are observed. Finite strains have also been shown to influence the martensite morphology [13,38,39].
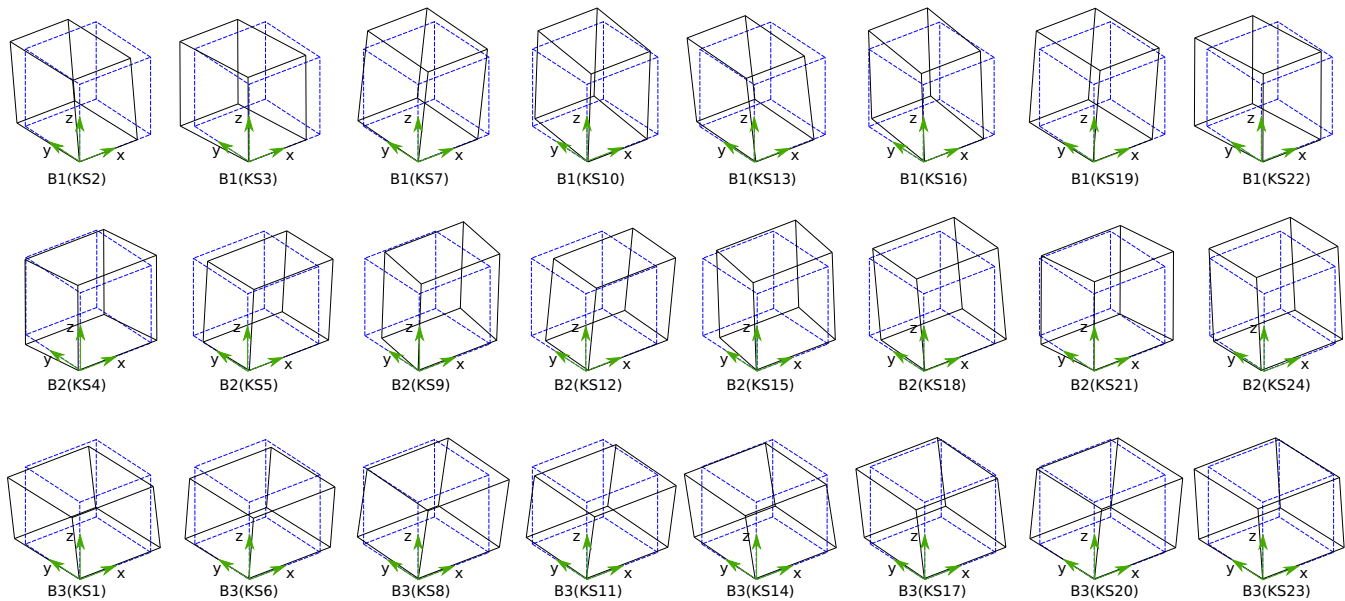
FIG. 12. Deformation of a unit cube for the 24 KS variants. The shear components of the strain tensor are $5\times$ magnified for better visualization. The blue dashed box represents the initial undeformed austenite configuration.

Finally, the use of the isotropic (homogenized) plasticity model could also influence the simulated morphologies. A finite-strain crystal plasticity approach that takes into account all martensite variants can overcome some of these shortcomings and is clearly a direction for further research. Although the simulations here are for idealized conditions, they provide physical insights that may be overlooked in macroscopic models. Traditionally, the problem of transformation-induced plasticity is studied using empirical constitutive models [7,9]. While these models have been successful in explaining many of the phenomena, they do not fully take into account the microstructural complexity associated with multivariant martensitic transformations. On the other hand, the analysis presented here naturally takes into account the thermodynamics of the phase transformation and can describe the complex microstructural evolution associated with transformation-induced plasticity in steel, without any empirical assumptions.

APPENDIX: DEFORMATION OF A UNIT CUBE FOR THE 24 KS VARIANTS

The deformed shape of a unit cube for all 24 KS variants listed in Table I is shown in Fig. 12. The shape change is plotted with reference to [0,0,0] of the shown coordinate system. Each row represents a KS variant with respect to its Bain strain variant B1, B2, or B3.

[1] H. Bhadeshia and R. Honeycombe, *Steels: Microstructure and Properties* (Butterworth-Heinemann, Amsterdam, 2017).

[2] A. G. Khachaturian, *Theory of Structural Transformations in Solids* (Dover Publications, New York, 1983).

[3] G. Krauss and A. R. Marder, The morphology of martensite in iron alloys, Metall. Trans. **2**, 2343 (1971).

[4] F. D. Fischer, G. Reisner, E. Werner, K. Tanaka, G. Cailletaud, and T. Antretter, A new view on transformation induced plasticity (trip), Int. J. Plast. **16**, 723 (2000).

[5] F. D. Fischer, Q.-P. Sun, and K. Tanaka, Transformation-induced plasticity (TRIP), Appl. Mech. Rev. **49**, 317 (1996).

[6] R. Mahnken, A. Schneidt, and T. Antretter, Macro modeling and homogenization for transformation induced plasticity of a low-alloy steel, Int. J. Plast. **25**, 183 (2009).

[7] G. W. Greenwood and R. H. Johnson, The deformation of metals under small stresses during phase transformations, Proc. R. Soc. London, Ser. A **283**, 403 (1965).

[8] C. L. Magee and H. W. Paxton, Transformation kinetics, microplasticity and aging of martensite in Fe-31Ni, Ph.D. thesis, Carnegie Inst. of Technology, Pittsburgh, Penn, 1966.

[9] J. B. Leblond, J. Devaux, and J. C. Devaux, Mathematical modeling of transformation plasticity in steels I: Case of ideal-plastic phases, Int. J. Plast. **5**, 551 (1989).

[10] A. W. Richards, R. A. Lebensohn, and K. Bhattacharya, Interplay of martensitic phase transformation and plastic slip in polycrystals, Acta Mater. **61**, 4384 (2013).

[11] Y. Wang and A. G. Khachaturyan, Three-dimensional field model and computer modeling of martensitic transformations, Acta Mater. **45**, 759 (1997).

[12] T. W. Heo and L.-Q. Chen, Phase-field modeling of displacive phase transformations in elastically anisotropic and inhomogeneous polycrystals, Acta Mater. **76**, 68 (2014).

[13] O. U. Salman, B. Muite, and A. Finel, Origin of stabilization of macrotwin boundaries in martensites, Eur. Phys. J. B **92**, 20 (2019).

[14] M. Bouville and R. Ahluwalia, Interplay between Diffusive and Displacive Phase Transformations: Time-Temperature-Transformation Diagrams and Microstructures, Phys. Rev. Lett. **97**, 055701 (2006).

[15] W. Zhang, Y. M. Jin, and A. G. Khachaturyan, Phase field microelasticity modeling of heterogeneous nucleation and growth in martensitic alloys, Acta Mater. **55**, 565 (2007).

[16] V. I. Levitas and A. M. Roy, Multiphase phase field theory for temperature- and stress-induced phase transformations, Phys. Rev. B **91**, 174109 (2015).

[17] M. Javanbakht and V. I. Levitas, Phase field simulations of plastic strain-induced phase transformations under high pressure and large shear, Phys. Rev. B **94**, 214104 (2016).

[18] X. H. Guo, S.-Q. Shi, and X. Q. Ma, Elastoplastic phase field model for microstructure evolution, Appl. Phys. Lett. **87**, 221910 (2005).

[19] R. Gröger, T. Lookman, and A. Saxena, Defect-induced incompatibility of elastic strains: Dislocations within the Landau theory of martensitic phase transformations, Phys. Rev. B **78**, 184101 (2008).

[20] R. Gröger, B. Marchand, and T. Lookman, Dislocations via incompatibilities in phase-field models of microstructure evolution, Phys. Rev. B **94**, 054105 (2016).

[21] H. K. Yeddu, A. Malik, J. Ågren, G. Amberg, and A. Borgenstam, Three-dimensional phase-field modeling of martensitic microstructure evolution in steels, Acta Mater. **60**, 1538 (2012).

[22] J. Kundin, D. Raabe, and H. Emmerich, A phase-field model for incoherent martensitic transformations including plastic accommodation processes in the austenite, J. Mech. Phys. Solids **59**, 2082 (2011).

[23] O. Shchyglo, G. Du, J. K. Engels, and I. Steinbach, Phase-field simulation of martensite microstructure in low-carbon steel, Acta Mater. **175**, 415 (2019).

[24] E. C. Bain, The nature of martensite, Trans. AIME **70**, 25 (1924).

[25] Z. Nishiyama, *Martensitic Transformations* (Academic Press, New York, 1978).

[26] G. Kurdjumow and G. Sachs, Über den mechanismus der stahlhärtung, Z. Phys. **64**, 325 (1930).

[27] O. Mustak, E. Evcil, and C. Simsir, Simulation of through-hardening of SAE 52100 steel bearings–Part I: Determination of material properties, Materialwiss. Werkstofftech. **47**, 735 (2016).

[28] F. Falk, Model free energy, mechanics, and thermodynamics of shape memory alloys, Acta Metall. **28**, 1773 (1980).

[29] K. Koumatos and A. Muehlemann, A theoretical investigation of orientation relationships and transformation strains in steels, Acta Crystallogr., Sect. A **73**, 115 (2017).

[30] A. Yamanaka, T. Takaki, and Y. Tomita, Elastoplastic phase-field simulation of self- and plastic accommodations in cubic→tetragonal martensitic transformation, Mater. Sci. Eng., A **491**, 378 (2008).

[31] D. A. Porter and K. E. Easterling, *Phase Transformations in Metals and Alloys*, 3rd ed., revised reprint (CRC Press, Boca Raton, 1992).

[32] H. K. Yeddu, T. Lookman, A. Borgenstam, J. Ågren, and A. Saxena, Martensite formation in stainless steels under transient loading, Mater. Sci. Eng., A **608**, 101 (2014).

[33] G. B. Olson and M. Cohen, *Dislocation Theory of Martensitic Transformations* (North-Holland, Amsterdam, 1986), Vol. 7, pp. 295–407.

[34] V. I. Levitas, A. V. Idesman, G. B. Olson, and E. Stein, Numerical modeling of martensitic growth in an elastoplastic material, Philos. Mag. A **82**, 429 (2002).

[35] A. Basak and V. I. Levitas, Nanoscale multiphase phase field approach for stress- and temperature-induced martensitic phase transformations with interfacial stresses at finite strains, J. Mech. Phys. Solids **113**, 162 (2018).

[36] A. Basak and V. I. Levitas, Interfacial stresses within boundary between martensitic variants: Analytical and numerical finite strain solutions for three phase field models, Acta Mater. **139**, 174 (2017).

[37] S. Chatterjee and H. K. D. H. Bhadeshia, Transformation induced plasticity assisted steels: Stress or strain affected martensitic transformation? Mater. Sci. Technol. **23**, 1101 (2007).

[38] V. A. Levin, V. I. Levitas, K. M. Zingerman, and E. I. Freiman, Phase-field simulation of stress-induced martensitic phase transformations at large strains, Int. J. Solids Struct. **50**, 2914 (2013).

[39] V. I. Levitas and M. Javanbakht, Interaction between phase transformations and dislocations at the nanoscale. Part 1. General phase field approach, J. Mech. Phys. Solids **82**, 287 (2015).